# Microcalorimeter measurement of x-ray spectra from a high-temperature magnetically confined plasma

M. E. Eckart, P. Beiersdorfer, G. V. Brown, et al.

## COLLECTIONS

Paper published as part of the special topic on Proceedings of the 23rd Topical Conference on High-Temperature Plasma Diagnostics

View Online      Export Citation      CrossMark

## ARTICLES YOU MAY BE INTERESTED IN

Read Now!

Review of Scientific Instruments

Special Issue: Advances in Measurements and Instrumentation Leveraging Embedded Systems

AIP Publishing

# Microcalorimeter measurement of x-ray spectra from a high-temperature magnetically confined plasma

M. E. Eckart,[1,a] ⓘ  P. Beiersdorfer,[1] ⓘ  G. V. Brown,[1] ⓘ  D. J. Den Hartog,[2] N. Hell,[1] ⓘ  R. L. Kelley,[3]
C. A. Kilbourne,[3] ⓘ  E. W. Magee,[1] ⓘ  A.-E. Y. Mangoba,[1] M. D. Nornberg,[2,b] ⓘ  F. S. Porter,[3] L. M. Reusch,[2,c]
and J. P. Wallace[2] ⓘ

## AFFILIATIONS

[1] Physics Division, Lawrence Livermore National Laboratory, Livermore, California 94550, USA
[2] Wisconsin Plasma Physics Laboratory, University of Wisconsin–Madison, Madison, Wisconsin 53706, USA
[3] X-ray Astrophysics Laboratory, NASA Goddard Space Flight Center, Greenbelt, Maryland 20771, USA

**Note:** Paper published as part of the Special Topic on Proceedings of the 23rd Topical Conference on High-Temperature Plasma Diagnostics.
[a] Author to whom correspondence should be addressed: eckart2@llnl.gov
[b] Current address: Department of Engineering Physics, University of Wisconsin–Madison, Madison, WI 53706, USA.
[c] Current address: Edgewood College, Madison, WI 53711, USA.

## ABSTRACT

A NASA-built x-ray microcalorimeter spectrometer has been installed on the MST facility at the Wisconsin Plasma Physics Laboratory and has recorded x-ray photons emitted by impurity ions of aluminum in a majority deuterium plasma. Much of the x-ray microcalorimeter development has been driven by the needs of astrophysics missions, where imaging arrays with few-eV spectral resolution are required. The goal of our project is to adapt these single-photon-counting microcalorimeters for magnetic fusion energy research and demonstrate the value of such measurements for fusion science. Microcalorimeter spectrometers combine the best characteristics of the x-ray instrumentation currently available on fusion devices: high spectral resolution similar to an x-ray crystal spectrometer and the broadband coverage of an x-ray pulse height analysis system. Fusion experiments are increasingly employing high-$Z$ plasma-facing components and require measurement of the concentration of all impurity ion species in the plasma. This diagnostic has the capability to satisfy this need for multi-species impurity ion data and will also contribute to measurements of impurity ion temperature and flow velocity, $Z_{eff}$, and electron density. Here, we introduce x-ray microcalorimeter detectors and discuss the diagnostic capability for magnetic fusion energy experiments. We describe our experimental setup and spectrometer operation approach at MST, and we present the results from an initial measurement campaign.

*Published under an exclusive license by AIP Publishing.* https://doi.org/10.1063/5.0043980

## I. INTRODUCTION

In research on magnetic fusion energy (MFE) devices, x-ray spectroscopy was developed early on as a powerful diagnostic for measuring fundamental plasma parameters and remains an indispensable tool for determining concentrations of multiple impurity ion species in the plasma core. This capability of x-ray spectroscopy is especially important now that plasma-facing components made of high-$Z$ metals are receiving increased consideration for use in burning plasma environments. Our work aims to apply detector technology developed by the astrophysics community to transform MFE x-ray diagnostics by providing a paradigm shift in spectroscopic capabilities. We have begun work toward adapting state-of-the-art x-ray microcalorimeter detector systems for MFE applications by installing and testing an existing microcalorimeter spectrometer, originally developed for astrophysics, under fusion-relevant plasma conditions at the Madison Symmetric Torus (MST).

Beiersdorfer *et al.* (2010)[1] introduced the anticipated performance of an x-ray microcalorimeter instrument for ITER. Such an

instrument was originally suggested as a complement to the ITER core imaging x-ray crystal spectrometer to mitigate risks, such as those associated with monitoring impurities in only a narrow spectral range as allowed by the crystal spectrometer design.[2] Here, we expand upon that initial work, and in Sec. II, we present a more detailed introduction to microcalorimeters and their basic operational principles and to the strengths, both scientific and technical, of using microcalorimeters as diagnostics for MFE devices. In Secs. III and IV, we describe the first phase of our diagnostic development work toward proving microcalorimeters for MFE, including preliminary results from our initial measurement campaign at MST. In Sec. V, we present an overview of the second phase of our diagnostic development work that will take place over the next three years, and Sec. VI provides a summary.

## II. BACKGROUND

### A. Overall characteristics of x-ray microcalorimeters

X-ray microcalorimeter spectrometers combine the best characteristics of the instrumentation currently available on fusion devices: the high spectral resolution of crystal spectrometers and broadband coverage provided by pulse-height analysis (PHA) systems. These instruments offer multi-keV spectral coverage: 0.1–12 keV is a typical operating range, which can easily be extended to much higher x-ray energies. Microcalorimeters are non-dispersive spectrometers, as opposed to crystal and grating spectrometers, and they have several advantages. For example, they are relatively easy to absolutely calibrate, and they only require a small access port to measure broadband line emission from impurities ranging from ions of Be to W. See Sec. II D for more details.

Originally driven by the needs of x-ray astrophysics missions, several research groups have developed these revolutionary x-ray detectors to enable imaging x-ray spectroscopy with relatively high spectral resolution. Although developed initially for observations from space, we have operated microcalorimeter spectrometers since 2000 on the EBIT-I electron beam ion trap device at Lawrence Livermore National Laboratory (LLNL).[3,4] This work is enabled by an ongoing collaboration between LLNL and the x-ray calorimeter group at NASA's Goddard Space Flight Center (GSFC). Our collaboration focuses on laboratory astrophysics and instrument testing and calibration. During the past two decades, we have employed GSFC-built calorimeters at the LLNL EBIT to study the x-ray emission from a variety of highly charged ions ranging from $B^{3+}$ to $W^{71+}$. Our collaboration's extensive use of calorimeters has in turn provided valuable feedback to the community on how to improve the functionality of these devices. Groups in Japan have also been active in both space- and ground-based calorimeter development and used an early instrument at a MFE device during two test campaigns.[5,6] More recently, a wider variety of x-ray microcalorimeter spectrometers and concepts have been developed for ground-based experiments, including at synchrotron light sources and other large facilities (see Refs. 7 and 8 and references therein).

### B. Basic operational principles of x-ray microcalorimeters

A microcalorimeter is a type of x-ray detector designed for high energy resolution, consisting of an x-ray absorber, a sensitive thermometer, and a weak link to a thermal bath (Fig. 1, left). The absorber converts the energy of an incoming x-ray to heat, thus raising the temperature of the absorber. Desired properties of the absorber are low heat capacity (to magnify the temperature rise) and high quantum efficiency. After photon absorption, the device cools through the weak link to reset for the next photon. Thermodynamic noise associated with the weak link means microcalorimeters work best at cryogenic temperatures. In addition to photons, microcalorimeter pixels are also sensitive to heat deposited by particles, including neutrons.

Several thermometer technologies currently under development rely on various semiconducting or superconducting material properties, including ion-implanted silicon thermistors and transition-edge sensors (TESs).

Instruments based on silicon thermistors are very mature, stable, near-turn-key systems that are robust against many environmental factors. The silicon thermistor instruments in use at LLNL use micro-machined ion-implanted silicon thermometers and HgTe x-ray absorbers. When a detector pixel absorbs an x-ray, a change in resistance causes a change in the voltage drop across the sensor, and the height of the corresponding voltage pulse is proportional to the energy of the photon. The equation for variable range hopping[9] describes the resistance in a doped semiconductor at low temperatures, albeit with some deviations reported.[10] The devices have high resistance, and a junction gate field-effect transistor (JFET) reads out each pixel individually. Arrays like those in Fig. 1 (right) use 10 $\mu$m-thick HgTe absorber tiles engineered to have low heat capacity, and devices routinely achieve better than 5 eV FWHM (full width at half maximum) energy resolution at 6 keV.[11]

In contrast, instruments based on TESs enable better energy resolution, larger array size, and higher count-rate capability. A TES exploits the narrow superconducting-to-normal-state transition of a thin metal film as an exceedingly sensitive thermometer. A small change in temperature in a TES creates a large change in resistance. TES microcalorimeters typically operate under voltage bias. An absorbed x-ray causes a brief increase in the TES resistance and thus a pulsed decrease in the device current. The height of the current pulse, measured by an inductively coupled SQUID ammeter, is proportional to the energy of the photon. The array in Fig. 2 uses a microns-thick Au/Bi absorber, designed to
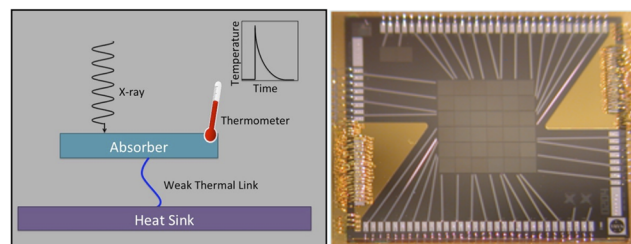


FIG. 1. (Left) Schematic of an x-ray microcalorimeter pixel and the pulse profile due to the heat of an incoming photon. (Right) Photo of a 36-pixel x-ray microcalorimeter array that flew on the *Hitomi* satellite.[11] The spectrometer we deployed at Madison Symmetric Torus (MST) in 2019 uses a similar array. Reproduced with permission from Kilbourne *et al.*, J. Astron. Telesc., Instrum., Syst. **4**(1), 011214 (2018). Copyright 2018 Author(s), licensed under a Creative Commons Attribution 4.0 License.
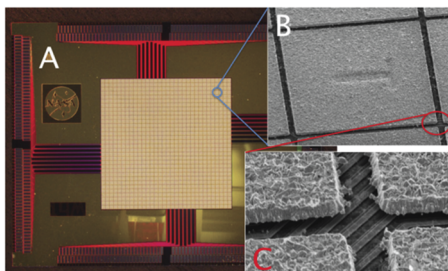
**FIG. 2.** Kilopixel TES microcalorimeter array built by the x-ray microcalorimeter group NASA/GSFC. Panel A shows the full array centered on the $15 \times 19$ mm$^2$ chip, with 256 pairs of wirebond pads at chip edge; B zooms in on a single pixel; and C highlights the overhanging absorbers and underlying bias wires.

thermalize the absorbed energy quickly, with a TES made from a Mo/Au proximity-effect bilayer. The bilayers are tuned to a transition temperature of $\approx 100$ mK, which is compatible with standard cryogenic platforms [e.g., adiabatic demagnetization refrigerators (ADRs) or dilution refrigerators].

These high filling-fraction, high quantum-efficiency TES microcalorimeter devices consistently achieve energy resolutions better than 2 eV FWHM at 6 keV.[12] These state-of-the-art results follow years of research in device physics and fabrication techniques by groups throughout the world. For the European-led Athena x-ray observatory (launch in the early 2030s),[13,14] NASA is currently designing arrays with identical pixel performance but higher pixel count (~3000 pixels) and a chip-size designed to accommodate bond pads for all pixels (3000 pad pairs). These large two-dimensional detector arrays enable larger fields of view for astrophysics applications, whereas, for applications that do not require imaging, such as many ground-based applications including fusion research, the increased pixel count translates to an increase in the total count-rate capability.

For a more detailed introduction to x-ray microcalorimeters, see Refs. 15 and 16.

### C. Scientific motivation for microcalorimeters as an x-ray diagnostic for MFE devices, including for burning plasmas

Because the energy resolution of TES microcalorimeters now rivals that of high-resolution x-ray crystal spectrometers, present-day TES calorimeters can, in principle, already measure the Doppler width of the lines emitted by impurity ions in burning plasmas. For example, the core ion and electron temperatures in ITER are expected to exceed 20 keV. In this case, the linewidth of the K-shell line of helium-like krypton, which had been proposed as an ITER ion temperature diagnostic,[17] is in excess of 10 eV, i.e., more than five times larger than the resolution of current TES detectors. The widths of L-shell tungsten lines also proposed as an ITER ion temperature diagnostic[2] are also multiple times that of the TES detector resolution.

In fact, calorimeters can, in principle, already be used to infer the core ion temperature of present-day plasmas heated with neutral beams or radio frequency power. Even at a temperature of only 4 keV (routinely achieved with auxiliary heating), the linewidths of

the K-shell lines of helium-like iron are still twice as large as the TES detector resolution, and the contribution from Doppler broadening is readily inferred. Note also that this high spectral resolution would be useful during the start-up phase of ITER, when high-power auxiliary heating will not be available and the electron temperature will be below 10 keV. For electron temperatures in the range of 2–10 keV, the line broadening for elements such as Ar and Fe will need to be recorded to provide the ion temperature. Furthermore, even a single line of sight through the plasma by an x-ray calorimeter can provide some information on the radial profile of the ion temperature, stemming from the capability of the calorimeter to simultaneously record emissions from multiple ion species and from the fact that the emissivity for each ion species peaks at a certain electron temperature. Using a separately measured electron temperature profile (e.g., from Thomson scattering), we can determine the approximate location where line radiation from each ion species was emitted. Correlating the ion temperature inferred from each linewidth with the plasma minor radius enables production of an approximate ion temperature profile (see Fig. 6 of Ref. 1).

In addition to the ion temperature and impurity species, a fusion plasma x-ray spectrum contains information about the ion flow velocity (from the Doppler shift of ion emission lines) and electron temperature and density. One of the more successful techniques, exploited in both astrophysical and fusion contexts, has been measurement of line intensity ratios involving forbidden or intercombination transitions.[18,19] In relatively low-density plasmas, such as the solar corona and MFE experiments, the population of excited levels that decay only via forbidden transitions can be high. For each forbidden line, a range of electron densities exists where electron collisions are comparable to the radiative decay rate.[20] In this range, changes in the electron density strongly affect the intensity of the forbidden lines. It is this feature that can be exploited as a plasma electron density diagnostic.

In MFE experiments, forbidden transitions are sometimes among the strongest x-ray emission lines, especially for high-$Z$ ions, such as tungsten, because of the scaling properties: forbidden transition probabilities scale as $Z^8$ or higher, whereas allowed electric dipole transition probabilities scale as $Z^4$.[21] An example of this situation is the bright unresolved Ni-like W feature observed at 7.93 Å in the ASDEX-U tokamak[22] that was resolved into two lines at the LLNL EBIT facility, one from an electric quadrupole transition and one from a magnetic octupole transition.[23] Modeling shows a large change in line ratio over the range of electron densities typical for a tokamak, making this pair of lines a candidate for robust $n_e$ measurements in present-day MFE experiments and in a substantial portion of ITER operational space.

As we have already noted, MFE research has shown renewed interest in x-ray measurements due to the use of molybdenum and tungsten as plasma-facing components and the associated issues with transport and confinement of these and other metals in all regions of the plasma, from the divertor region to the plasma core. For example, a crucial area of fusion research is understanding energy and particle losses from the core plasma due to radiation, radial transport, and various instabilities. Core impurity accumulation studies are of special importance in this context, as even small amounts of a high-$Z$ impurity in the core can dramatically degrade plasma confinement. X-ray measurements are needed to quantify the influx and accumulation of impurities in the core plasma and,

thus, to understand the impact of plasma–surface interactions with tungsten, molybdenum, or other plasma-facing components on the core plasma. Because calorimeters simultaneously record x rays from all impurities with $Z \geq 4$ and with high resolution limited mainly by the plasma Doppler motion, they offer an unprecedented opportunity to absolutely quantify species-resolved impurity concentrations in the plasma as a function of time and provide much-needed data for transport simulations. Bringing x-ray diagnostics into the x-ray calorimeter age is timely to properly support the utilization of high-$Z$ plasma-facing materials in the progression toward producing burning plasmas.

## D. Technical advantages of microcalorimeters over existing diagnostics

Microcalorimeters are non-dispersive spectrometers, as opposed to crystal and grating spectrometers, a characteristic that provides several advantages: the energy resolution does not degrade with the source size and the instruments are easy to align, have high quantum efficiency, and are straightforward to calibrate. Another key advantage for future MFE applications is their small port-access requirement. Such spectrometers will only require an ~25 mm diameter radial sightline through the core of a high-temperature fusion plasma, and the instrument itself can be placed tens of meters away.[1] The small plasma viewing window means microcalorimeters offer orders of magnitude lower neutron hazard compared to crystal spectrometer designs (e.g., see Fig. 1 of Ref. [1]). The microcalorimeter dewar and electronics rack can be placed far from the plasma vessel and behind significant shielding, and the instrument itself would be serviceable. For example, Fig. 3 shows a simple model of our calorimeter dewar installed at MST. In this case, the dewar is only 4 m from the plasma vessel, but that distance could be significantly increased in larger fusion devices, and would likely only be limited by space constraints (e.g., the size of experiment hall or building). This configuration also lends to easily adding a microcalorimeter to a small viewport auxiliary to a crystal spectrometer (or other) port on a large fusion experiment.
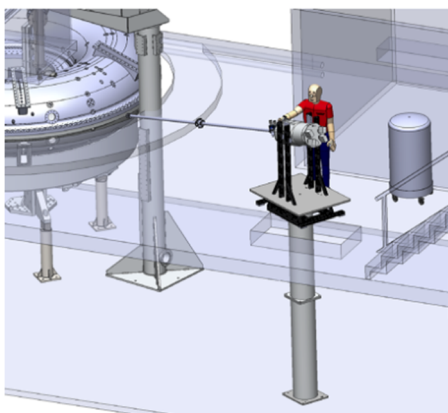


**FIG. 3.** A simple model of the x-ray calorimeter as currently installed on MST. The calorimeter views the plasma through a small diameter flight tube 4 m in length and is mounted on a damping column to eliminate acoustic coupling to the detector.

Finally, the x-ray microcalorimeter spectrometer represents a type of passive measurement technique that may be critical for the next generation of fusion devices, such as ITER's successor, the DEMOnstration power plant (DEMO). Port access for diagnostics will be extremely limited in these devices, and techniques that rely on the injection of particle or photon beams into the plasma (such as interferometry, Thomson scattering, and charge-exchange recombination spectroscopy) will be extremely challenging or impossible.[24,25] Thus, the diagnostic challenge will shift to a need to implement passive diagnostics that measure plasma parameters by recording emission from the plasma, such as the x rays produced by impurities. Developing microcalorimeter spectrometers for MFE devices directly addresses this diagnostic challenge.

## III. EXPERIMENTAL DIAGNOSTIC DEVELOPMENT WORK

In 2017, we began our program to implement and test x-ray microcalorimeter spectrometry in an MFE experiment, to address challenges in adapting such instruments to the MFE pulsed-plasma environment. Our original intent was to install an instrument on NSTX-U or DIII-D; however, construction and upgrade efforts at these facilities reduced the availability of these devices for development of x-ray calorimetry. Instead, we established a strong collaboration with University of Wisconsin–Madison researchers and aimed to perform tests at MST. In this section, we describe our work that resulted in deploying and operating a microcalorimeter spectrometer at MST in 2019.

### A. MST overview

MST is a toroidal magnetic plasma confinement device typically operated as a reversed-field pinch (RFP).[26] MST is a flexible experiment facility able to produce fusion-relevant plasma conditions with electron temperatures up to 2 keV at an electron density of $10^{19}$ m$^{-3}$. The major and minor radii of the device are 1.5 and 0.5 m. The typical fuel gas is deuterium, and a variety of noble gases can be introduced as impurity dopants. Graphite and aluminum are the main plasma-facing surfaces, and thus, C and Al are the dominant impurities. Large amounts of data can be collected over a variety of plasma conditions, as the equilibrium flat-top period of each plasma discharge is 10–30 ms long and ~100 discharges are produced in a typical run day. The daily run schedule can be very flexible, and, for example, researchers can gain access to the experiment floor between shots.

### B. Instrument for initial measurement campaign

The microcalorimeter instrument we chose to deploy from LLNL to MST for our initial measurement campaign has a 32-pixel detector array based on silicon thermistors. We used this instrument, known as the XRS/EBITv2 (XRS for short), as a facility instrument at the Livermore EBIT-I until 2007,[27] and in 2011 and 2012 for campaigns at the Linac Coherent Light Source (LCLS) x-ray-free electron laser at SLAC.

The XRS has $625 \times 625 \times 8 \ \mu m^3$ HgTe absorbers, each mounted on a doped silicon thermistor. Each pixel is independently wired. We typically operate the detector with a heatsink temperature of ≈60 mK, achieved using an adiabatic demagnetization refrigerator
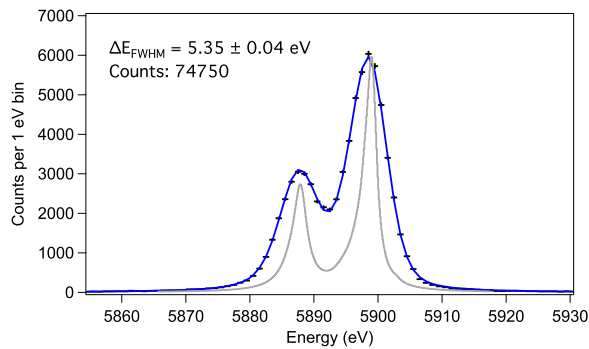
**FIG. 4.** Measured x-ray spectrum acquired using an $^{55}$Fe source at LLNL in June 2019. The blue curve is the best fit to data, assuming Gaussian broadening, and the gray curve indicates the natural line shape of the Mn K$\alpha$ complex.[28,29]
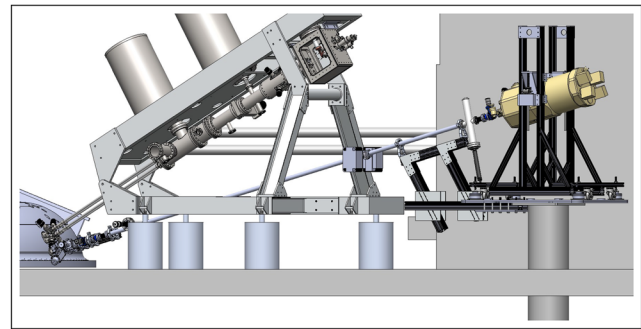


**FIG. 6.** This figure accompanies Fig. 5, showing a solid model of the main components of the experimental setup at MST.

(ADR) installed in an IR Labs dewar. The system requires a pumped liquid helium bath, as well as a liquid nitrogen shield. The detector views the source out of the bottom (long end) of the dewar through four aluminized polyimide infrared blocking filters, which have been photometrically calibrated. The quantum efficiency of the HgTe absorbers was also calibrated prior to instrument assembly.

The XRS is operated using the same software and duplicates of the hardware developed for space flight instruments. The main components are the calorimeter analog processor (CAP), computers used for digital processing of the photon pulses, and computer-controlled housekeeping electronics to read out and control thermometers and the ADR. The system is fully automated and capable of real-time processing of x-ray spectra.

In spring 2019, pre-ship tasks were completed at LLNL, including re-assembly of the electronics, testing of the assembled instrument, and calibration using an $^{55}$Fe radioactive source and the LLNL EBIT-I. The x-ray emission from mainly He-like and H-like ions created using EBIT-I is ideal for calibrating the energy gain scale and

line-spread function of the instrument. Figure 4 illustrates the high spectral resolution of the XRS, showing a best-fit combined resolution of 5.35 eV FWHM at 5.9 keV, with per-pixel resolutions ranging from 4.7 to 6.3 eV.

## C. Experimental setup at MST

Other pre-ship work included selection of a port at MST and design of an instrument stand, external filter stack, and beam–tube assembly needed to interface with MST. Accelerometer data taken during MST discharges have confirmed substantial vibration at acoustic frequencies produced by the transformer components and partially transferred to the vacuum vessel and mounting structure. Therefore, vibration isolation was a priority in the mechanical design of the pillar assembly upon which the XRS is mounted. The beam–tube assembly incorporated a series of filters to allow definition of the spectral waveband and apertures to provide an energy-independent reduction in x-ray flux.

Installation of the XRS at MST took place in summer 2019. The beam–tube assembly and instrument stand shipped to MST in June
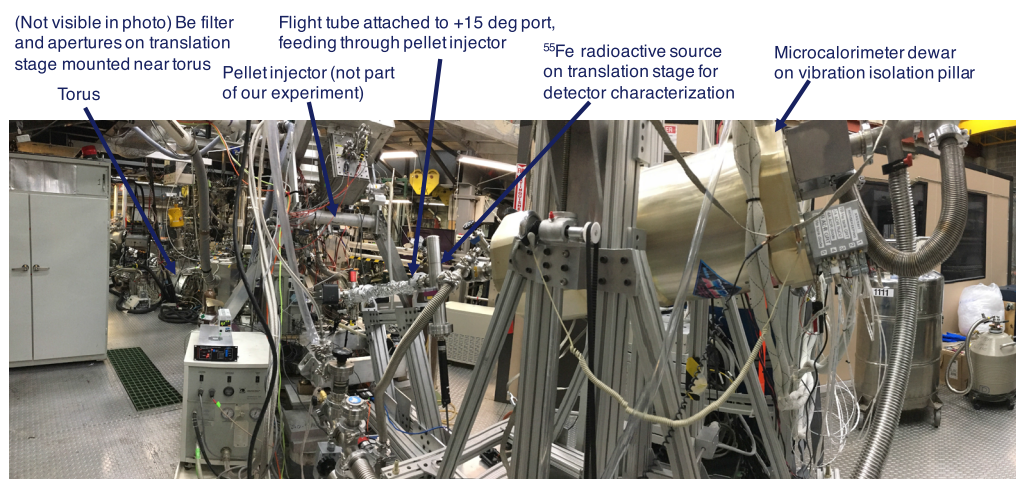


**FIG. 5.** GSFC/LLNL XRS microcalorimeter installed at MST in July 2019.

2019 and were installed and attached to a facility vibration isolation pillar. In July, the calorimeter instrument shipped to MST, and following installation underwent a post-shipment checkout using a radioactive calibration source. The heatsink temperature stability in this post-shipment checkout was better than that at LLNL, indicative of the good vibration isolation provided by the pillar assembly. Figures 5 and 6 illustrate this implementation of the XRS at MST. The measured instrument spectral resolution was slightly degraded compared to the tests at LLNL (Fig. 4), with a combined spectral resolution of 6.5 eV FWHM at 5.9 keV and per-pixel resolutions ranging from 4.9 to 8.1 eV. This change is due to two factors: increased 60 Hz noise and a low calibration-source flux that limited our ability to track and correct small temporal changes in the gain. Both of these factors are straightforward to address, and we expect this small degradation will be eliminated in the next experimental campaign.

## IV. DATA ACQUISITION AND FIRST-LIGHT RESULTS

First-light experiments during MST discharges took place in August 2019, during which the XRS recorded x-ray spectra of photons emitted by Al impurity ions. This first-light campaign employed a range of MST plasma conditions, combined with various beam tube filters and apertures, to achieve specific count rates. For most of the acquisition sequences, the combination of plasma conditions and optical path was targeted to achieve $\sim 1$ ct pixel$^{-1}$ shot$^{-1}$ to ensure the data had the highest achievable spectral resolution. The tests incorporated the MST trigger signal into the microcalorimeter data acquisition system and analysis confirmed that each photon arrival was time-tagged relative to the MST discharge trigger with an uncertainty of <1 ms and that the x-ray signal appeared when expected relative to the discharge profile (see Fig. 7). Most microcalorimeter systems in existence do not use an external timing trigger (e.g., for astronomy or many beamline applications); however, the experience using spectrometers equipped with an external trigger at the LLNL EBIT proved invaluable in quickly achieving these results.

These data are informative regarding how the electromagnetic and acoustic noise of an MFE experiment affects the instrument performance. The raw data showed evidence of interference (likely electrical, possibly magnetic) consistent with the "sawtooth" features routinely observed during MST discharges due to magnetic reconnection events; however, the interference signal was small compared to the x-ray pulse signal and had minimal overlap with our signal bandpass and thus has limited effect on the spectral resolution. In addition to electrical or magnetic pickup, resolution can be degraded by fluctuations in the detector heatsink temperature, which can be thought of roughly as causing time-dependent fluctuations in each pixel's gain. The heatsink temperature of the XRS, which we controlled at 58.50 mK, showed only small (<0.05 mK) disruptions during the discharge owing to the good vibration isolation provided by the pillar assembly.

The number of photons in the example spectra (Fig. 8) is limited because of the short initial data run. However, even given the low number of counts and degraded resolution due to small gain uncertainties, the calorimeter spectra allow initial probes of physical mechanisms. For example, comparison to calculations shows that the spectra have much lower charge balances than would naively
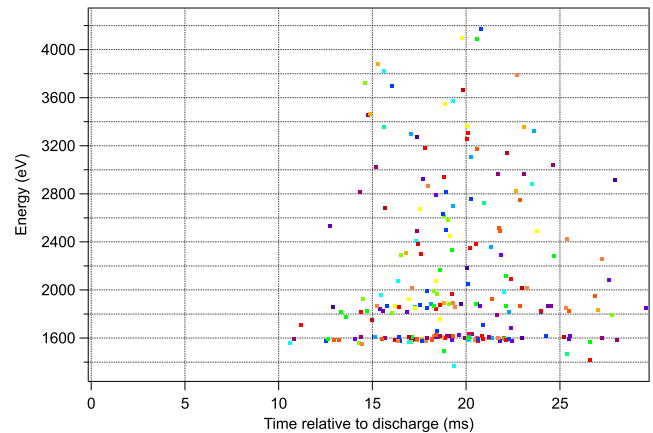


**FIG. 7.** First-light data illustrating the effective time-tagging of XRS events relative to the MST discharge trigger. Every dot represents a time-tagged x-ray photon event, each the result of real-time processing of an 164 ms digitized record. Different colors indicate different pixels. These data confirm that the signals appear when expected: for $\sim 8$ ms per shot, from $\sim 15-23$ ms after discharge, for this particular MST discharge profile. There is some variation, e.g., the MST diagnostics saw flux to 27 ms on one shot.

be expected. The spectrum of the 400 eV plasma (blue curve) likely has significant contributions from lower charge states of Al than the model (black curve)—Be-like and B-like Al features have peaks at 1560 and 1545 eV, and the pulsed parallel current drive (PPCD) spectrum (green curve) lacks the strong hydrogen-like Al emission lines present in similar models of 600 eV plasma. These differences are related to charge exchange with neutrals, which is a significant
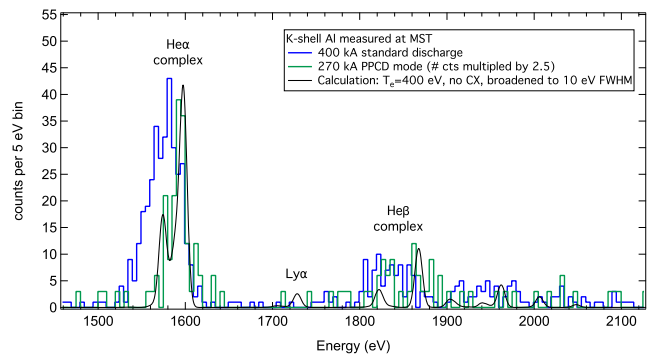


**FIG. 8.** Initial spectra showing lines emitted from Al impurity ions. The blue curve shows data from 90 discharges where the MST temperature is $\sim 400$ eV; the green curve shows data from 30 discharges where MST is in PPCD mode with an average temperature of 600 eV (with the total number of counts multiplied by 2.5 for ease of comparison). Individual pixels showed $\sim 6$ eV spectral resolution, but the geometry of the $^{55}$Fe source in the beam tube prohibited simultaneous gain tracking and pixel-to-pixel gain alignment, and thus, the combined spectra show broadening, likely due to long-term gain drift with a possible contribution from short-term (near-discharge) gain changes. This issue will be addressed during our upcoming experimental campaign. The black curve shows a calculation using the Flexible Atomic Code (FAC)[30] assuming an electron density of $10^{19}$ m$^{-3}$, and the labels highlight the dominant features of the model curve. The He$\alpha$ and He$\beta$ features include emission from He-like and lower charge states.
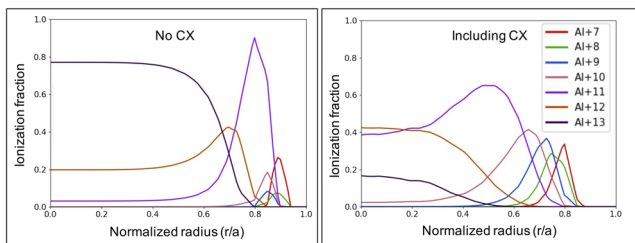
**FIG. 9.** An example of the dramatic difference in the modeled ionization-fraction balance at MST in the PPCD mode when accounting for charge exchange with neutral hydrogen. The calculations assume $T_e$ = 1500 eV and use typical values for the neutral density. Reprinted with permission from P. D. VanMeter, "Observations of helical plasma dynamics using complementary x-ray diagnostics in the MST," Ph.D. thesis, University of Wisconsin–Madison, 2020.[31]

effect at MST: Fig. 9 shows an example of the difference in the modeled ionization-fraction balance at MST when incorporating charge exchange. MST does not have a divertor so the effect is heightened, but even a small neutral population can affect plasma and can be relevant at many MFE devices. Microcalorimeter spectra can quickly assess charge balance for impurity ions across the waveband of interest.

## V. FUTURE WORK

Considering continued construction and upgrade efforts at both DIII-D and NSTX-U and advantages we have found in the flexibility afforded by deploying our instruments to a mid-size physics experiment, we plan to continue developing x-ray calorimetry for application as a fusion diagnostic at MST over three upcoming campaigns, one per year. The first two campaigns will use the XRS that is currently deployed at MST. For the final campaign, once we have fully assessed the operating environment of the calorimeter and implemented required changes, we will deploy a TES-based spectrometer, as such an instrument is more suitable for the high-count rates produced at MFE facilities. This work includes verifying our

neutron mitigation scheme that will be needed for use on larger fusion experiments. Completion of our future work will resolve critical issues and establish a path for implementation on fusion facilities, including ITER.

Similar to x rays, incident neutrons can cause a rise in the temperature of the microcalorimeter absorbers, which may result in contamination of the x-ray signals. In addition, neutrons impinging on the detector substrate could cause unwanted noise or low-level signals in one or more pixels. To prevent undue heating of the array by neutrons, the x-ray flux from the plasma must be deflected by a grazing incidence mirror. For installation of a microcalorimeter on a burning plasma device, we plan to arrange the geometry of the mirror such that the deflected x-ray flux proceeds to the detector, while shielding material absorbs the undeflected neutron flux (Fig. 10). The mirror will deflect the incoming x rays by about 0.5°. To test this method of neutron protection on MST, we will install a grazing incidence mirror in the x-ray calorimeter flight tube. This deflection means that, over a 4 m distance, the incoming neutron beam (defined by the initial collimating aperture before being bent by the grazing-incidence mirror) will be separated from the x-ray beam by about 3.5 cm. This separation should be sufficient to keep unscattered neutrons from hitting the microcalorimeter array.

Operated as an RFP, MST is an extremely flexible source of D–D neutrons (2.5 MeV). At low plasma currents, the neutron flux is below the scintillator detector limit. At high plasma currents, the neutron production reaches $10^{11}$ s$^{-1}$ immediately following magnetic reconnection events. The reconnection events produce a suprathermal deuterium population.[32] The D–D fusion cross section is extremely sensitive to ion energy, so a small number of fast ions can contribute more to the total neutron flux than the entire thermal population, and, in fact, the fast ions completely dominate neutron production in standard MST RFP plasmas. In addition to standard RFP operation, we can operate MST in a high-confinement mode into which we can inject a 1 MW deuterium neutral beam. This mode of operation can produce neutrons at a rate of up to $10^{12}$ s$^{-1}$ (integrated over the entire plasma and into all directions).
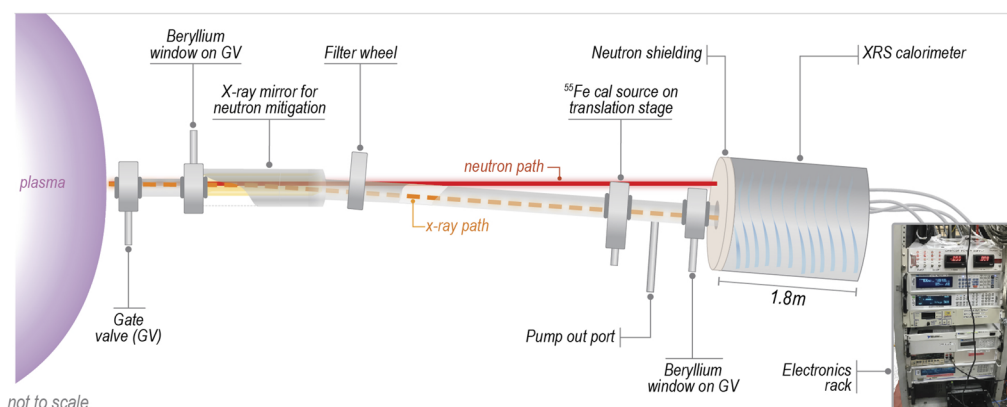


**FIG. 10.** Rough conceptual layout for the neutron mitigation scheme that we plan to test in 2022 at MST. The vacuum beam tube (< 4 in. diameter) connects the plasma vessel to the XRS and allows for operation with or without the mirror. We can select waveband and count-rate incident on the detector array by choice of aperture (not pictured here) and filters (both motorized) and mirror position. The x-ray mirror deflects the beam by 0.5° over 4 m for a 3.5 cm separation.

At this neutron rate, approximately ten neutrons would impact each pixel of the unshielded XRS microcalorimeter detector during each MST discharge, which is more than sufficient to test the neutron mitigation method described above. Standard high-current RFP discharges with a peak neutron rate of $10^{11}$ s$^{-1}$ are probably more suitable for these tests, since approximately one neutron will impact each pixel of the XRS during a discharge.

Although our upcoming experimental work will take place at MST, we plan to continue our ongoing discussions with diagnostics teams at DIII-D and NSTX-U and to begin preparing for installation on such facilities in the near future, based on lessons learned from the measurement campaigns on MST. While our research gains tremendously from using existing spectrometers developed primarily by NASA for space missions and often using spare or prototype detector components, several aspects of the detector and system design should be optimized specifically for MFE diagnostic requirements. We plan to lay out a conceptual design for a system appropriate for ITER or for an experiment such as JT-60SA. Building such an instrument for fusion application will leverage the decades of development by NASA and other agencies. However, building this instrument will require (at least) a dedicated design and fabrication run. For ground-based instrumentation, as compared to space-based instruments, many requirements can be relaxed, allowing much greater design flexibility, particularly in the array (fill fraction) and readout (multiplex factor) architecture. A combination of increased array size (number of pixels) and decreased detector pulse time constant allows a higher counting rate but taxes the multiplier electronics. We plan to study such tradeoffs and may choose a modular detector assembly, possibly with separate arrays optimized for different x-ray energy ranges, coupled to a microwave SQUID multiplexer.[33] We could reasonably implement these alterations in a short time, since, compared to space missions, aspects such as instrument volume, mass, and power needs are not constrained.

## VI. SUMMARY

In this paper we provide an introduction to high-resolution x-ray microcalorimeter spectrometers and scientific and technical advantages of using these instruments as x-ray diagnostics for burning plasmas. We present our experimental diagnostic development work to date, having deployed and operated a microcalorimeter spectrometer at MST, as well as our plans for development over the next few years. This diagnostic development is consistent with the needs of the fusion and plasma science community as highlighted during the recent plasma physics community planning process (CPP). The cross-cut measurement and diagnostics section of the CPP report[34] describes the need for high-resolution x-ray spectroscopy of high-Z elements: "High-resolution x-ray imaging spectroscopy of impurities is critical . . .. The needed instrumentation advancements include improved spectral resolution, broader spectral coverage, and higher time resolution, ideally with small port access requirements and small equipment footprint."

## DATA AVAILABILITY

The data that support the findings of this study are available from the corresponding author upon reasonable request.

## REFERENCES

[1] P. Beiersdorfer, G. V. Brown, J. Clementson, J. Dunn, K. Morris, E. Wang, R. L. Kelley, C. A. Kilbourne, F. S. Porter, M. Bitter, R. Feder, K. W. Hill, D. Johnson, and R. Barnsley, Rev. Sci. Instrum. **81**, 10E323 (2010).

[2] P. Beiersdorfer, J. Clementson, J. Dunn, M. F. Gu, K. Morris, Y. Podpaly, E. Wang, M. Bitter, R. Feder, K. W. Hill, D. Johnson, and R. Barnsley, J. Phys. B: At. Mol. Phys. **43**, 144008 (2010).

[3] M. A. Levine, R. E. Marrs, J. R. Henderson, D. A. Knapp, and M. B. Schneider, Phys. Scr. **T22**, 157 (1988).

[4] F. S. Porter, P. Beiersdorfer, G. V. Brown, M. F. Gu, R. L. Kelley, S. Kahn, C. A. Kilbourne, and D. B. Thorn, J. Phys.: Conf. Ser. **163**, 012105 (2009).

[5] K. Shinozaki, A. Hoshino, Y. Ishisaki, U. Morita, T. Ohashi, T. Mihara, K. Mitsuda, K. Tanaka, Y. Yagi, H. Koguchi, Y. Hirano, and H. Sakakita, Nucl. Instrum. Methods Phys. Res., Sect. A **559**, 760 (2006).

[6] K. Shinozaki, A. Hoshino, Y. Ishisaki, U. Morita, T. Ohashi, T. Mihara, K. Mitsuda, K. Tanaka, Y. Yagi, H. Koguchi, Y. Hirano, and H. Sakakita, Rev. Sci. Instrum. **77**, 043104 (2006).

[7] W. B. Doriese, P. Abbamonte, B. K. Alpert, D. A. Bennett, E. V. Denison, Y. Fang, D. A. Fischer, C. P. Fitzgerald, J. W. Fowler, J. D. Gard, J. P. Hays-Wehle, G. C. Hilton, C. Jaye, J. L. McChesney, L. Miaja-Avila, K. M. Morgan, Y. I. Joe, G. C. O'Neil, C. D. Reintsema, F. Rodolakis, D. R. Schmidt, H. Tatsuno, J. Uhlig, L. R. Vale, J. N. Ullom, and D. S. Swetz, Rev. Sci. Instrum. **88**, 053108 (2017).

[8] K. M. Morgan, Phys. Today **71**(8), 28 (2018).

[9] A. L. Efros and B. I. Shklovskii, J. Phys. C: Solid State Phys. **8**, L49 (1975).

[10] J. Zhang, W. Cui, M. Juda, D. McCammon, R. L. Kelley, S. H. Moseley, C. K. Stahle, and A. E. Szymkowiak, Phys. Rev. B **48**, 2312 (1993).

[11] C. A. Kilbourne, J. S. Adams, R. P. Brekosky, J. A. Chervenak, M. P. Chiao, M. E. Eckart, E. Figueroa-Feliciano, M. Galeazzi, C. Grein, C. A. Jhabvala, D. Kelly, M. A. Leutenegger, D. McCammon, F. Scott Porter, A. E. Szymkowiak, T. Watanabe, and J. Zhao, J. Astron. Telesc., Instrum., Syst. **4**, 011214 (2018).

[12] M. Durkin et al., "Demonstration of Athena X-IFU compatible 40-row time-division-multiplexed readout," in IEEE Transactions on Applied Superconductivity, August 2019 (IEEE, Piscataway, NJ, 2019), Vol. 29, pp. 1–5.

[13] D. Barret et al., Proc. SPIE **10699**, 106991G (2018).

[14] F. Pajot, D. Barret, T. Lam-Trong, J.-W. den Herder, L. Piro, M. Cappi, J. Huovelin, R. Kelley, J. M. Mas-Hesse, K. Mitsuda, S. Paltani, G. Rauw, A. Rozanska, J. Wilms, M. Barbera, F. Douchin, H. Geoffray, R. den Hartog, C. Kilbourne, C. Le Du, C. Macculi, J.-M. Mesnager, and P. Peille, J. Low Temp. Phys. **193**, 901 (2018).

[15] C. K. Stahle, D. McCammon, and K. D. Irwin, Phys. Today **52**(8), 32 (1999).

[16] K. Irwin and G. Hilton, "Transition-edge sensors," in Cryogenic Particle Detection, edited by C. Enss (Springer, 2006), pp. 63–150.

[17] R. Barnsley, M. O'Mullane, L. C. Ingesson, and A. Malaquias, Rev. Sci. Instrum. **75**, 3743 (2004).

[18] A. H. Gabriel and C. Jordan, Mon. Not. R. Astron. Soc. **145**, 241 (1969).

[19] H. Griem, "Principles of plasma spectroscopy," in Cambridge Monographs on Plasma Physics (Cambridge University Press, 1997).

[20] Y. Ralchenko, I. N. Draganić, D. Osin, J. D. Gillaspy, and J. Reader, Phys. Rev. A **83**, 032517 (2011).

[21] H.-J. Kunze, Introduction to Plasma Spectroscopy (Springer, 2009), Vol. 56.

[22] R. Neu, K. B. Fournier, D. Bolshukhin, and R. Dux, Phys. Scr. **T92**, 307 (2001).

[23] J. Clementson, P. Beiersdorfer, and M. F. Gu, Phys. Rev. A **81**, 012505 (2010).

[24] A. J. H. Donné, A. E. Costley, and A. W. Morris, Nucl. Fusion **52**, 074015 (2012).

[25] F. P. Orsitto, R. Villari, F. Moro, T. N. Todd, S. Lilley, I. Jenkins, R. Felton, W. Biel, A. Silva, M. Scholz, J. Rzadkiewicz, I. Duran, M. Tardocchi, G. Gorini, C. Morlock, G. Federici, and A. Litnovsky, Nucl. Fusion **56**, 026009 (2016).

[26] L. Marrelli, P. Martin, M. E. Puiatti, J. S. Sarff, B. E. Chapman, J. R. Drake, D. F. Escande, and S. Masamune, Nucl. Fusion **61**, 023001 (2021).

[27] F. S. Porter, G. V. Brown, K. R. Boyce, R. L. Kelley, C. A. Kilbourne, P. Beiersdorfer, H. Chen, S. Terracol, S. M. Kahn, and A. E. Szymkowiak, Rev. Sci. Instrum. **75**, 3772 (2004).

[28] G. Hölzer, M. Fritsch, M. Deutsch, J. Härtwig, and E. Förster, Phys. Rev. A **56**, 4554 (1997).

[29] G. Hölzer and F. S. Porter, "Correction and extension to hölzer *et al.*," private communication (2004).

[30] M. F. Gu, Can. J. Phys. **86**, 675 (2008).

[31] P. D. VanMeter, "Observations of helical plasma dynamics using complementary x-ray diagnostics in the MST," Ph.D. thesis, University of Wisconsin–Madison, 2020.

[32] R. M. Magee, D. J. den Hartog, S. T. A. Kumar, A. F. Almagri, B. E. Chapman, G. Fiksel, V. V. Mirnov, E. D. Mezonlin, and J. B. Titus, Phys. Rev. Lett. **107**, 065005 (2011).

[33] J. A. B. Mates, D. T. Becker, D. A. Bennett, B. J. Dober, J. D. Gard, J. P. Hays-Wehle, J. W. Fowler, G. C. Hilton, C. D. Reintsema, D. R. Schmidt, D. S. Swetz, L. R. Vale, and J. N. Ullom, Appl. Phys. Lett. **111**, 062601 (2017).

[34] S. Baalrud, N. Ferrano, L. Garrison, N. Howard, C. Kuranz, J. Sarff, E. Scime, W. Solomon *et al.*, "A community plan for fusion energy and discovery plasma sciences," Report of the 2019–2020 American Physical Society Division of Plasma Physics Community Planning Process, 2020.